Long-Term Near-Infrared Compound Variability of Three Recently Discovered Brown Dwarfs in IC 348 and NGC 1333

Ruby Lark Mendelsund[1, a)] and Tom Rice[2, b)]

[1]*Department of Astronomy, Columbia University, 538 West 120th Street, New York, New York 10027, USA*
[2]*American Astronomical Society, 1667 K Street NW, Suite 800, Washington, DC 20006, USA*

[a)] Corresponding author: rm3529@columbia.edu
[b)] tom.rice@aas.org

Abstract. While much is known about stars, less is known about brown dwarfs: cool, low-mass, substellar byproducts of star formation. Studying the photometric behavior of brown dwarfs is an important strategy to better understand their dynamics as well as their atmospheric and intrinsic features. We positionally matched two United Kingdom Infrared Telescope (UKIRT) observing campaigns in the Perseus region to previously published brown dwarf catalogs and established the presence of 10 and 6 sources with reported spectral types of M6 or later in IC 348 and NGC 1333, respectively. We assessed the long-term ($\gtrsim$8 month) near-infrared (*J*, *H*, and *K* band) variability of these 16 sources by analyzing their individual reduced chi-squared values, their Stetson indices, and their periodicity, and found two variable brown dwarfs in IC 348—one of which is a periodic variable—and one in NGC 1333. We propose three different explanations for the observed periodicity and variability by drawing upon current literature. This paper is a companion paper to Rice et al. (2025, *in prep*).

INTRODUCTION

Brown dwarfs (BDs) are objects of increasing astrophysical interest. BDs are classified by a few salient criteria: masses between 0.013 $M_\odot$ (or perhaps lower, as is suggested by Vos et al. in [1]) and 0.08 $M_\odot$; a lack of hydrogen fusion, though they are believed to fuse deuterium (and, in some cases, lithium); and low effective temperatures that continue to become cooler over time [2]. BDs are a natural consequence of the star formation process, and much less is known about their intrinsic properties and behaviors compared to what is known about stars (stellar isochrones, for example, make divergent predictions about what happens in the BD mass regime [3]).

The mass range encompassed by BDs make them particularly valuable to both stellar and planetary astrophysicists. Young BDs are of great interest to stellar astrophysicists given their crucial placement in the stellar evolution sequence [4]. Low-mass BDs are of great interest to planetary astrophysicists given that BDs may be analogs for exoplanets [1].

One scientific approach taken to better understand BDs is to study their photometric variability—how the brightness of these sources varies over time. Variability monitoring of this kind can be a window into the formation and dynamics of these young objects; the presence of disks (and whether or not there is active accretion from the disk onto the surface); the presence of cold or hot spots; rotation rates and angular momentum evolution; and atmospheric physics such as the presence of clouds, dust, etc. Near-infrared (NIR) variability studies of this kind have been performed before on young stars [5, 21], as well as on BDs in the many megayear (Myr) to gigayear (Gyr) age [6, 7]. Studies on young BDs in particular (1–10 Myr) have been performed by Cody and Hillenbrand [4, 8, 9], Scholz and Jayawardhana [10], and Rebull et al. [11, 12]. Very few long-term (more than 100 days) NIR variability studies focused specifically on brown dwarfs have been performed.

In this paper, we present the NIR variability of young, low-mass sources in NGC 1333 and IC 348. Two observation campaigns were carried out toward these regions in the *J*, *H*, and *K* NIR bands from mid-2012 to mid-2015, making our work one of the longest-term NIR variability studies of BDs to date. These observations have allowed us to identify three variable brown dwarfs, one of which is a periodic variable. This paper, which focuses on the very faintest known and most recently discovered (i.e., post-2016) BD members in these two clusters, is a companion to Rice et al. (2025, *in prep*), which examines over 500 BDs and very low-mass stars whose status had been affirmed in Luhman et al. [16].

METHODS AND OBSERVATIONS

Survey Descriptions, Selection of Reference Catalogs, Variability Selection, and Analysis

The data in this paper were taken from surveys of the young star-forming regions IC 348 and NGC 1333 in Perseus collected on the United Kingdom Infrared Telescope (UKIRT), located atop Mauna Kea in Hawaii. Each night of observations included observations in the NIR *J, H,* and *K* bands, which correspond to 1.1–2.2 μm. More information on the telescope and data processing can be found in the Appendix. Ninety percent completeness limits for this specific data set are shown in Table 2 of the Appendix.

We selected confirmed BDs from the catalogs of Esplin and Luhman [13], Allers and Liu [14], and Luhman and Hapich [15]; details on the selection and positional matching process are in the Appendix. A forthcoming article (Rice et al., 2025, *in prep*) treats BDs identified by Luhman et al. in [16]. We found 16 positional matches; of these, nine were previously designated members and BDs by [16]. We present the spatial distributions of these sources, plotted against our UKIRT sources, as well as a Hertzsprung-Russell diagram with a 2-Myr isochrone from Baraffe et al. [17] in Figs. 4–6 of the Appendix, respectively. We used spectral-type-to-temperature models from Luhman et al. [18] and Herczeg and Hillenbrand [33], as well as a 2-Myr isochrone from Baraffe et al. [17] to generate mass estimates for all objects (shown in Table 4 of the Appendix).

We selected a given object as variable if it met at least two of the three following criteria: (a) a reduced chi-squared value exceeding $\chi^2_\nu = 3$ in all three photometric bands, (b) a three-band Stetson variability index [19] exceeding 1, and (c) found to be periodic via a Lomb-Scargle periodicity analysis [20]. Histograms of the reduced chi-squared values for both regions, plots of the Stetson indices, and descriptions of all three of these statistical measures can be found in the Appendix.

RESULTS AND DISCUSSION

We performed variability analysis on the 16 objects in our sample; of these, we identified three as variable. A summary of these results is shown in Table 5 of the Appendix. Of the three variables, two are in IC 348 (UHW J056.01221 +31.87436 and UHW J055.98976 +32.24691, here abbreviated J056 and J055, respectively), and one is in NGC 1333 (UHW J052.43392 +31.32982, here abbreviated J052). One of the two variables in IC 348 is periodic. An analysis and discussion of this sample's statistical variability properties appear in the Appendix.

We interpreted the three-band *JHK* light curves for our three variables from three distinct perspectives to determine (or constrain) the physical origin(s) of variability in each source: (1) the morphology of each light curve, (2) the presence or absence of periodicity, and (3) color. Two of the three variables—J056 and J052—have confirmed infrared excesses [16], indicating that they are disked. Their variability is aperiodic with high peak-to-peak amplitudes, which is consistent with variability from disked objects.

The two disked objects show substantial color variability alongside their brightness variability. Typically, we group color variability into *redder-when-dimmer* events, which we generally interpret (following [21] and subsequent studies of NIR variability in young stellar objects) as variability arising from dust occultation, and *redder-when-brighter* events (equivalently *bluer-when-fainter*), which (again following [21, 5] and related studies) we interpret as arising from changes in the geometry of the warm, infrared-emissive inner disk. Following [5], we use the term "compound variability" to describe variability associated with an object that sequentially exhibits both *redder-when-dimmer* and *redder-when-brighter* events.

Nonperiodic variable J056 in IC 348, shown in Fig. 1, was identified by Allers and Liu in [14]. It has a reported spectral type of M6 and an estimated mass between 0.03 and 0.04 solar masses. Arrows (A) trace through a brief dip in brightness apparent in all three bands, though the dip is markedly steepest at the *J* band. As such, this is a *redder-when-dimmer* event. This event is especially conspicuous in the *K*, *J–K* color-magnitude diagram, where it stands out as a plunge to the lower right, in a direction parallel to an ISM dust reddening vector. By contrast, arrows (B) trace through a *redder-when-brighter* event, in which the *K* band is becoming fainter while the *J* band remains relatively unchanged; in other words, the *J-K* difference decreases alongside *K* band dimming. In summation, this object is a compound variable whose behavior in color-magnitude space is nonlinear and whose physical behavior cannot be constrained to just one process.

Nonperiodic variable J052 in NGC 1333 is shown in Fig. 2. It has a reported spectral type of M8 and an estimated mass of about 0.02 solar masses. As with variable object J056, its light curve shows compound variability, as illustrated by color-coded arrows.

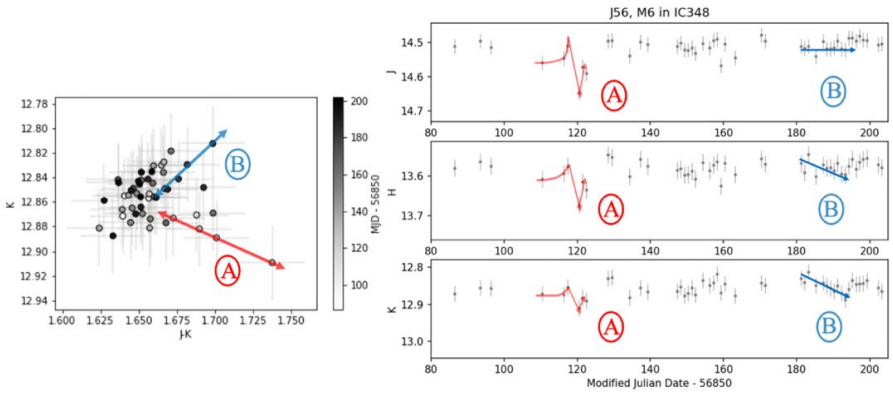

(a) (b)

FIGURE 1. Color-magnitude diagram (a) and *JHK* light curve (b) for variable J056. Typical photometric errors are displayed for each data point as error bars. Two noteworthy epochs are labeled with color-coded arrows and the labels "A" and "B"; note their distinct slopes in *K, J–K* color-mag space. Here, we have only shown a portion of the light curve.

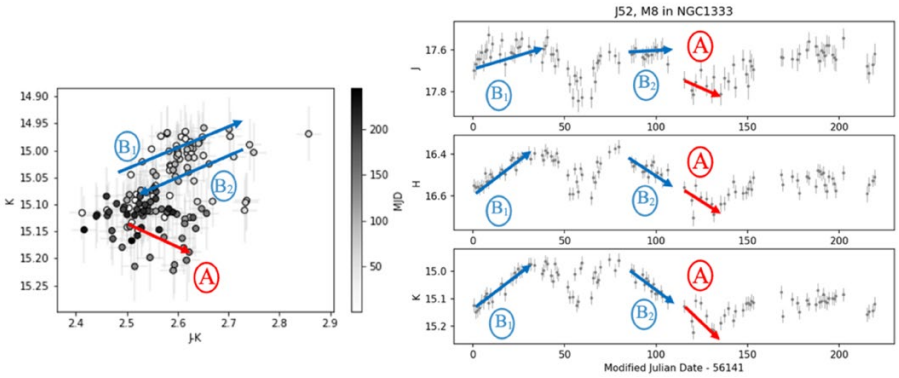

(a) (b)

FIGURE 2. Color-magnitude diagram (a) and *JHK* light curve (b) for variable J052. Typical photometric errors are displayed for each data point as error bars. Three noteworthy epochs are labeled with color-coded arrows and the labels "A" and "B," following the convention used in Fig. 1.

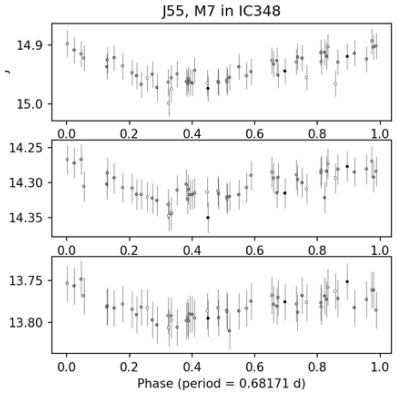

FIGURE 3. A phase-folded *JHK* light curve and color-magnitude diagram for periodic variable J055. Typical photometric errors are displayed for each data point as error bars, and a periodogram of this star's light curve appears in the Appendix (Fig. 11).

Periodic variable J055 is reported by Allers and Liu [14] as having a spectral type of M7 ([16] reported M6) and being very low gravity, with an estimated mass of between 0.02 and 0.03 solar masses. The period we observed for UHW J055 in IC 348 was ~0.68 days or ~16.32 hours. Its periodogram appears in the Appendix as Fig. 11. The nearly sinusoidal nature of the phase-folded light curve (shown in Fig. 3), as well as the amplitude of variability (also reported

in Table 5 of the Appendix), is consistent with the physical origin of variability being hot/dark spots rotating in and out of view. This period of this object, 0.68 days, is consistent with the period distribution of other similar BD studies such as [6], adding confidence to our inference that this object is a rotating BD with a period that is typical for objects of its class.

CONCLUSION

From our monitoring study of 16 known low-mass objects, we identified three variables. Of these, two (reported by [16] to have infrared excesses consistent with disks) are aperiodic variables, and one is periodic with hot/cool spots. In each of the disked variables, we observe variability with divergent color-magnitude slopes (i.e., "compound variability") when these objects are monitored for a sufficiently long time. This behavior connects the variability of brown dwarfs with their stellar-mass YSO siblings, adding to our knowledge of the earliest stages of brown dwarfs.

ACKNOWLEDGMENTS

We thank the Columbia University Department of Astronomy for supporting this research project, Johanna Vos for her thoughtful guidance and valuable discussions, and Bo Reipurth for sharing the UKIRT data with us.

REFERENCES

1. J. M. Vos, J. K. Faherty, J. Gagné, M. Marley, S. Metchev, J. Gizis, E. L. Rice, and Kelle Cruz, Astrophys. J. **924**, 68 (2022).
2. B. R. Oppenheimer, S. R. Kulkarni, and J. R. Stauffer, "Brown Dwarfs," in *Protostars and Planets IV*, edited by V. Mannings, A. Boss, and S. Russell (University of Arizona Press, Tucson, AZ, 1998).
3. J. R. Najita, G. P. Tiede, and J. S. Carr, Astrophys. J. **31**, 1534 (1999).
4. A. M. Cody and L. A. Hillenbrand, Astrophys. J. **191**, 389 (2010).
5. T. S. Rice, B. Reipurth, S. J. Wolk, L. P. Vaz, and N. J. G. Cross, Astron. J. **150**, 132 (2015).
6. J. M. Vos, B. Biller, K. N. Allers, J. K. Faherty, M. C. Liu, S. Metchev, S. Eriksson, E. Manjavacas, T. J. Dupuy, M. Janson, et al., Astron. J. **160**, 38 (2020).
7. J. M. Vos, B. A. Biller, M. Bonavita, S. Eriksson, M. C. Liu, W. M. J. Best, S. Metchev, J. Radigan, K. N. Allers, M. Janson, et al., Mon. Not. R. Astron. Soc. **483**, 1 (2019).
8. Ann Marie Cody and Lynne A. Hillenbrand, Astrophys. J. **741**, 9 (2011).
9. Ann Marie Cody and Lynne A. Hillenbrand, Astrophys. J. **796**, 129 (2014).
10. Alexander Scholz and Ray Jayawardhana, Astrophys. J. **638**, 1056 (2006).
11. L. M. Rebull, J. R. Stauffer, A. M. Cody, L. A. Hildebrand, T. J. David, and M. Pinsonneault, Astron. J. **155**, 196 (2018).
12. L. M. Rebull, J. R. Stauffer, A. M. Cody, L. A. Hillenbrand, J. Bouvier, N. Roggero, and T. J. David, Astron. J. **159**, 273 (2020).
13. T. L. Esplin and K. L. Luhman, Astron. J. **154**, 134 (2017).
14. K. N. Allers and M. C. Liu, Publ. Astron. Soc. Pac. **132**, 104401 (2020).
15. K. L. Luhman and C. J. Hapich, Astron. J. **160** 57 (2020).
16. K.L. Luhman, T. L. Esplin, and N.P. Loutrel, Astrophys. J. **827**, 52 (2016).
17. I. Baraffe, D. Homeier, F. Allard, and G. Chabrier, Astron. Astrophys. **577**, A42 (2015).
18. K. L. Luhman, J. R. Stauffer, A. A. Muench, G. H. Rieke, E. A. Lada, J. Bouvier, and C. J. Lada, Astrophys. J. **593**, 1093 (2003).
19. P. B. Stetson, Publ. Astron. Soc. Pac. **108**, 851 (1996).
20. William H. Press and George B. Rybicki, Astron. J. **338**, 277 (1989).
21. J. M. Carpenter, L. A. Hillenbrand, and M. F. Skrutskie, Astron. J. **121**, 3160 (2001).
22. M. Casali, A. Adamson, C. Alves de Oliveira, O. Almaini, K. Burch, T. Chuter, J. Elliot, M. Folger, S. Foucaud, N. Hambly, et al., Astron. Astrophys. **467**, 777 (2007).
23. J. Bally, J. Walawender, D. Johnstone, H. Kirk, and A. Goodman, "The Perseus Cloud," in Handbook of Star Forming Regions, Vol. I, Astronomical Society of the Pacific Conference Series, edited by B. Reipurth (ASPCS, Provo, UT, 2008), p. 308.
24. W. Herbst, "Star Formation in IC 348," in Handbook of Star Forming Regions, Vol. 1, Astronomical Society of the Pacific Conference Series, edited by B. Reipurth (ASPCS, Provo, UT, 2008), pp. 72, 375.
25. S. Ghosh, S. Mondal, S. Dutta, R. Das, S. Joshi, S. Lata, D. Khata, and A. Panja, Mon. Not. R. Astron. Soc. **500**, 5106 (2020).
26. G. N. Ortiz-León, L. Loinard, S. A. Dzib, P. A. B. Galli, M. Kounkel, A. J. Mioduszewski, L. F. Rodríguez, R. M. Torres, L. Hartmann, A. F. Boden, et al., Astrophys. J. **865**, 73 (2018).
27. C. Zucker, E. F. Schlafly, J. S. Speagle, G. M. Green, S. K. N. Portillo, D. P. Finkbeiner, and A. A. Goodmanet, Astrophys. J. **869**, 83 (2018).
28. S. T. Hodgkin, M. J. Irwin, P. C. Hewett, and S. J. Warren, Mon. Not. R. Astron. Soc. **394**, 675 (2009).
29. B. A. Wilking, M. R. Meyer, T. P. Greene, A. Mikhail, and G. Carlson, Astron. J. **127**, 1131 (2004).
30. K. L. Luhman, Annu. Rev. Astron. Astrophys. **50**, 65 (2012).
31. M. Morales-Calderón, J. R. Stauffer, L. A. Hillenbrand, R. Gutermuth, I. Song, L. M. Rebull, P. Plavchan, J. M. Carpenter, B. A. Whitney, K. Covey, et al., Astrophys. J. **733**, 50 (2011).
32. Jacqueline Radigan, Astrophys. J. **797**, 120 (2014).
33. G. Herczeg and L. Hillenbrand, Astrophys. J. **786**, 97 (2014).
34. J. VanderPlas, ApJSS **236**, 16 (2018).
35. Astropy Collaboration, A. M. Price-Whelan, P. L. Lim, N. Earl, N. Starkman, L. Bradley, D. L. Shupe, A. A. Patil, L. Corrales, C. E. Brasseur, et al., Astrophys. J. **935**, 167 (2022).

APPENDIX

UKIRT/WFCAM Data and Processing

The data in this paper were taken from surveys of the young star-forming regions IC 348 and NGC 1333 in Perseus collected on the United Kingdom Infrared Telescope (UKIRT), located atop Mauna Kea in Hawaii at 4194 m elevation. The two surveys were carried out using the WFCAM instrument, which is described by Casali in [22]. These WFCAM observations covered a 53 × 53 arcmin field with coordinate centers described in Table 1. Each night of observations included observations in the NIR *J*, *H*, and *K* bands, which correspond to 1.1–2.2 μm. The frequency of these observations was irregular (due to weather and other scheduling considerations), with observations clustered as often as once per night. The IC 348 survey in particular spanned multiple observing seasons, requiring at least one gap in observations during a period in which the Sun's position led to a months-long gap in observations. Further details on these surveys are in Table 1.

The UKIRT/WFCAM data cleaning and processing are described in detail in [5]; we refer the reader to that paper for more information.

TABLE 1. Descriptions of the two monitoring surveys carried out by WFCAM on UKIRT and estimated physical properties of the two regions.

Source Name	Center Coordinates (J2000)		Estimated Distance	Estimated Age	Obs. Start	Obs. End	No. of Obs.	ΔT (days)
	R.A.	Decl.						
IC 348	3:44:36.1	+32:12:34	300 ± 15 pc	2–6 Myr	2014-7-11	2015-7-30.	85	384
NGC 1333	3:28:49.5.	+31:17:10	299 ± 14 pc	1–2 Myr	2012-8-12	2013-4-4	171	235

IC 348 and NGC 1333 are both star clusters in the Perseus molecular cloud, described in detail in [23]. A summary of essential features of both clusters is in Table 1. IC 348 is located in the eastern corner of the Perseus cloud complex, at a distance of approximately 300±15 pc [24]. Its age is estimated as somewhere from 2 to 6 Myr [24, 18]. A similar photometric variability study was performed on IC 348 in optical *I*-band by Ghosh et al. [25]. NGC 1333, a bright reflection nebula in the western section of the Perseus cloud, is, as of now, considered the most active of the star-forming regions within Perseus [24]. Its distance is suggested by Ortiz-León et al. as 293 ± 22 pc, based on data taken from Gaia parallaxes [26]. Zucker et al. report a similar distance of 299 ±14 pc in [27]. Its age has been estimated in the 1−2-Myr range by Herbst et al. [24].

TABLE 2. UKIRT 90% completeness limits in each band.

Photometric Band	Completeness Limit
J	18.7
H	18.4
K	17.9

The estimates of photometric uncertainties in the pipeline-produced UKIRT data catalogs were somewhat too optimistic. To remedy this, following Rice et al. in [5], we calibrated the photometric uncertainties (i.e., the error bars) in these surveys using the prescription presented in Hodgkin et al. in [28], resulting in a minimum night-to-night error of around 0.02 mag. The UKIRT surveys have approximate 90% completeness limits—the magnitudes at which any fainter object has below a 90% chance of being detected—as designated in Table 2. We disregarded sources whose magnitudes were fainter than these values. When analyzing the light curves, sources that presented faulty or erroneous photometry were also disregarded.

Selection of Reference Catalogs

Catalogs of known BD members of IC 348 and NGC 1333 were selected based on three primary criteria: (a) overlap in sky coverage with the UKIRT surveys, (b) publication after [16], and (c) inclusion of spectroscopic follow-up confirming BD status.

We selected catalogs with spectroscopic classifications because mass estimates from photometric data alone are less reliable: while mass estimates can be derived from photometric data alone, spectroscopic follow-up confirming effective temperatures of sources is more reliable when establishing BD status, especially given certain signatures of youth, such as presence of water absorption bands in the cool photospheres of young BDs, as is discussed by Wilking et al. in [29] and Luhman et al. in [30].

We selected three reference catalogs that met these criteria:

(1) Esplin and Luhman [13] is a comprehensive survey in the Taurus and Perseus molecular clouds using photometry from 2MASS, the *Spitzer Space Telescope*, the United Kingdom Infrared Telescope Infrared Deep Sky Survey, Pan-STARRS1, the Sloan Digital Sky Survey (SDSS), *Gaia*, and the *Wide-field Infrared Survey Explorer* (*WISE*). It is also a spectroscopic follow-up to [16] that includes spectroscopic data from SpeX.

(2) Allers and Liu [14] combines photometry from the UH 88-inch telescope and spectroscopy from SpeX to establish BDs in Perseus and Ophiuchus. Sources that underwent spectroscopic follow-up include both candidate members flagged by [16] as well as candidates flagged by their own photometric analysis, most notably the implementation of a custom near-IR filter.

(3) Luhman and Hapich [15] combines photometry from Hubble's WFC3 and NIR spectroscopy from Gemini to identify BDs in IC 348.

We took BDs to be those with spectral types of M6 or later (as is established in [13]). Any source in our selected reference catalog, even if it was a match, was not considered if its spectral type was earlier than M6.

All sources with spectral types later than M6 from each catalog were individually positionally matched against the appropriate UKIRT survey. We limited the results of this process to matches that were within 0.3 arcseconds of each other to minimize false positive identifications. Results from the positional matching are shown in Table 3. In IC 348, there were 29 total sources from all three catalogs; we found 10 positional matches, shown in Fig. 4. In NGC 1333, there were 12 total sources from all three catalogs; we found six positional matches, which are shown in Fig. 5. Matched sources from both catalogs are shown in a Hertzsprung-Russell (i.e., color-magnitude) diagram presented as Fig. 6. A description of the properties of all 16 matched sources, including their names, spectral types, and estimated masses, is given in Table 4.

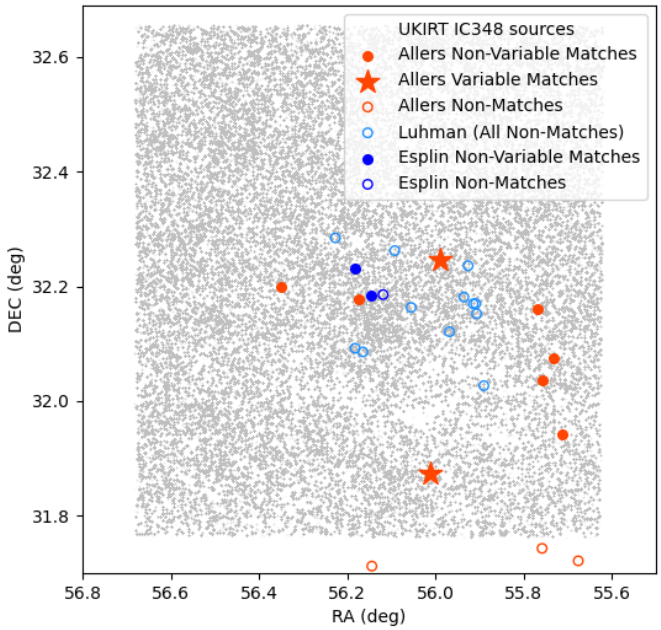

FIGURE 4. Spatial distribution of sources in this study in IC 348. UKIRT sources are shown in gray and display the extent of our observed field in IC 348. Allers and Liu [14], Esplin and Luhman [13], and Luhman and Hapich [15] identified 29 substellar sources in this region, 26 of which are displayed here. Of the three not shown, one is designated as "other" and described in Table 3; the remaining two are outside our observing field. Of the 26 sources shown above and within our field, 10 are positional matches to the UKIRT dataset, designated by closed circles. We identified two of those 10 matches as variable.

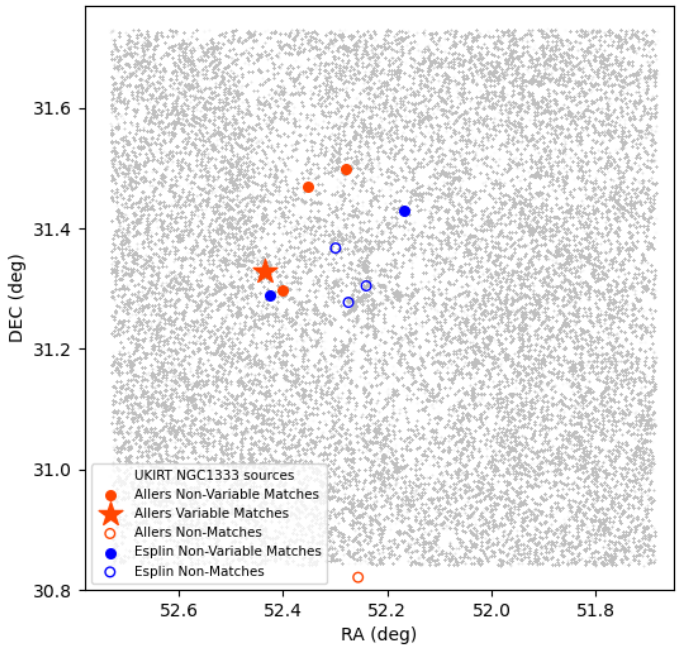

FIGURE 5. Spatial distribution of sources included in this study in NGC 1333. UKIRT sources are shown in gray and display the extent of our observed field in NGC 1333. Allers and Liu [14] and Esplin and Luhman [13] identify 12 substellar sources in this region, 10 of which are displayed here. Of the two not shown, one is designated as "other" and described in Table 3; the remaining one is outside our observing field. Of the 10 sources shown above and within our field, six are positional matches to the UKIRT dataset, designated by closed circles. We identified one of those six matches as variable.

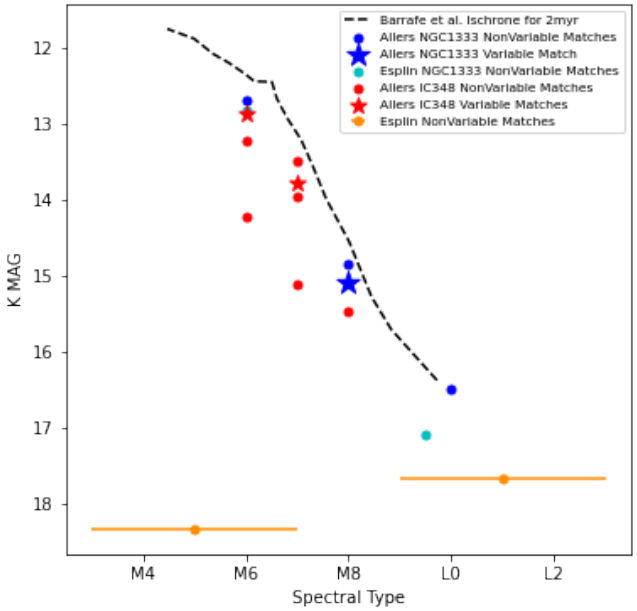

FIGURE 6. The Hertzsprung-Russell diagram for the 16 positionally matched sources in IC 348 and NGC 1333. The three variable matches are shown as stars; nonvariable matches are shown as closed circles. Esplin IC 348 matches (in orange) have spectral types described as "Mid-M" and "M9-L3"; error bars depict this uncertainty. The isochrone for 2 Myr, which we limited to objects with masses between 0.01 and 0.2 solar masses, is taken from Baraffe et al. in [17] and shown as a black dotted line. The isochrone is distance-adjusted assuming d = 300 pc (μ = 7.39) and ends at spectral type ~L0. The K magnitudes of BDs shown here are not corrected for extinction, and so it is unsurprising that many of them lie beneath the isochrone; that none of them lie above it may be taken as evidence that the adopted distance is approximately correct.

Nonperiodic Variability Analysis

Reduced chi-squared (χ_ν^2) is a statistic that measures how variable a star's light curve is relative to its level of noise in individual photometric bands (*J, H*, and *K* in this case). It is given by chi-squared over degrees of freedom, as is shown in the following formula:

$$\chi_\nu^2 = \frac{\chi^2}{n-1}, \tag{1}$$

where n is the number of valid photometric measurements in that band, and the chi-squared (χ^2) is given by

$$\chi^2 = \sum_{n=1}^{N} \frac{(m_i - \bar{m})^2}{\sigma_i^2}, \tag{2}$$

where m_i is the magnitude in the photometric band for a given epoch i, $\bar{m}$ is the mean magnitude in the photometric band across all observations, and σ_i is the observational uncertainty. A similar process is used by Carpenter et al. in [21]. We treated sources with $\chi_\nu^2 > 3$ as potentially variable. Given normally distributed errors, a nonvariable source should have χ_ν^2 approaching 1; any variety of modest common deviations from perfectly normally distributed error will bias the source's χ_ν^2 to values slightly higher than 1. Thus, any source with variability of amplitude greater than the pipeline-generated error bars will have a χ_ν^2 significantly greater than 1; these are the sources we treated as potentially variable following Carpenter et al. in [21].

Histograms of the χ_ν^2 values measured for all sources in IC 348 and NGC 1333 are shown in Figs. 7 and 8, respectively, with the 16 matched brown dwarfs studied here highlighted in blue.

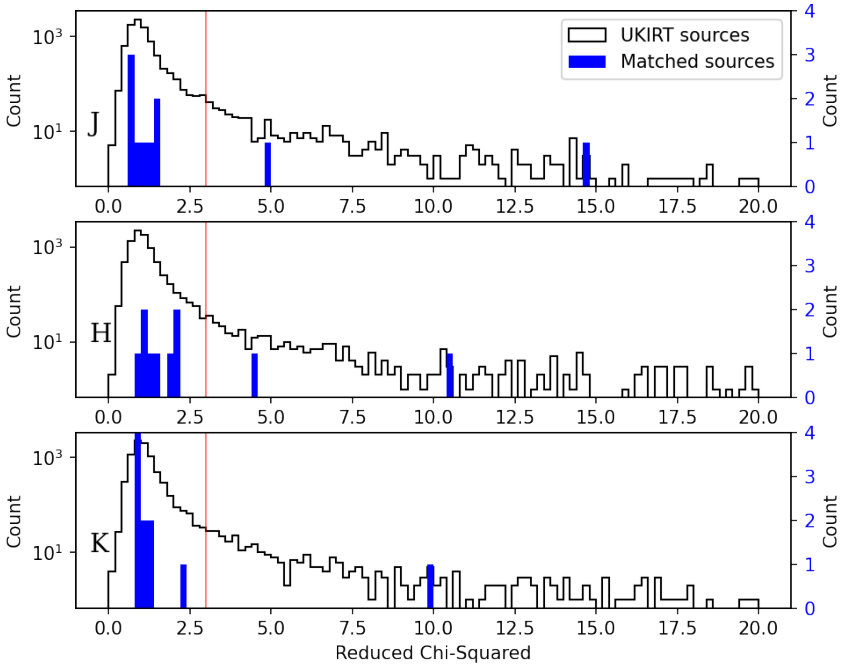

FIGURE 7. Histograms of χ_ν^2 values for IC 348. All UKIRT IC 348 sources are shown in white, with count shown on the leftmost *y* axis. All matched sources are shown in blue, with count shown in the blue, rightmost *y* axis. A red line at $\chi_\nu^2 = 3$ designates the cutoff for variable sources.

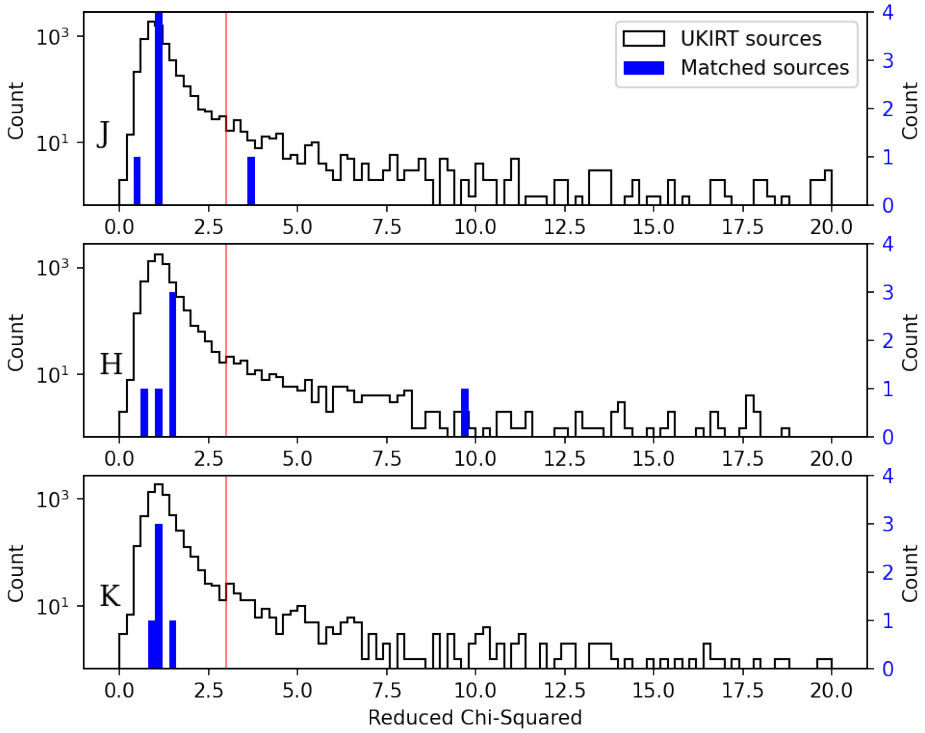

FIGURE 8. Histograms of χ_ν^2 values for NGC 1333. All UKIRT NGC 1333 sources are shown in white, with count shown on the leftmost *y* axis. All matched sources are shown in blue, with count shown in the blue, rightmost *y* axis. A red line at $\chi_\nu^2 = 3$ designates the cutoff for variable sources.

Occasional, non-Gaussian sources of noise (such as weather concerns) do arise in our photometric measurements frequently enough (even after the data-cleaning process), such that we avoided formally labeling sources as variable based simply on their χ^2_ν values. We performed additional analysis using the Stetson variability index, which assesses simultaneous, correlated variability across all three bands and was first defined in [19]. The major advantage to using the Stetson index for variability analysis of this kind is that it is the most likely to reveal true physical mechanisms of variability given its cross-band correlation [21]. The index *S* is defined as follows:

$$S = \frac{\sum_{i=1}^{p} g_i \,\mathrm{sgn}\,(P_i)\sqrt{|P_i|}}{\sum_{i=1}^{n} g_i}, \tag{3}$$

where p is the number of pairs of simultaneous observations of a given source, g_i gives the weight associated with each pair, $P_i = \delta_{j(i)}\,\delta_{k(i)}$ is the product of the normalized residuals of two observations, and the normalized residual δ_i in each band is given by

$$\delta_i = \sqrt{\frac{n}{n-1}}\frac{m_i - \bar{m}}{\sigma_i}, \tag{4}$$

where n is the number of observations in that band, m_i is the magnitude at epoch i, σ_i is the photometric error on m_i, and $\bar{m}$ is the source's mean magnitude in that band. When simultaneous photometric measurements are taken in three bands, the weight g_i is set to ⅔ for each pair of measurements.

Plots of the Stetson index as a function of *K* magnitude for all sources in IC 348 and NGC 1333 are shown in Figs. 9 and 10, respectively, with the 16 matched brown dwarfs studied here highlighted in blue.

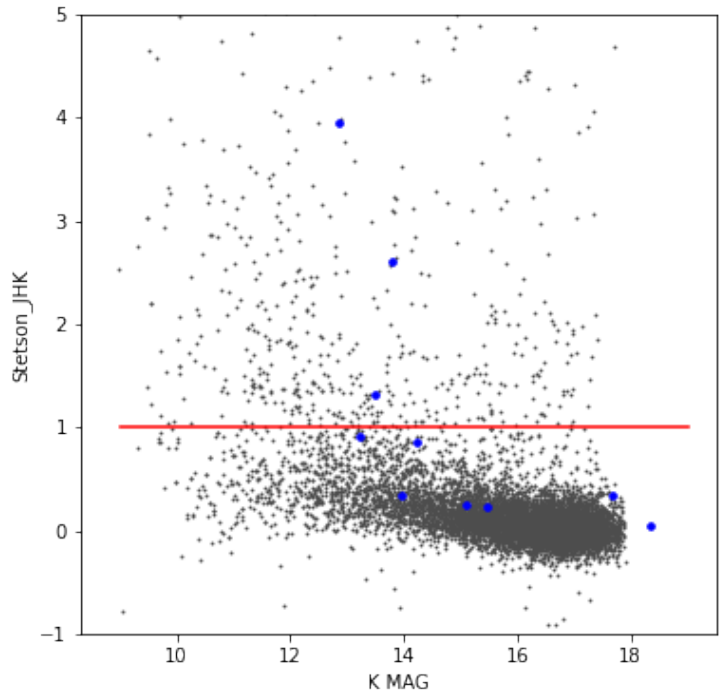

FIGURE 9. Plot of *JHK* Stetson variability index vs *K* magnitude in IC 348. All UKIRT sources are shown in gray; all matched sources are shown in blue. A red line at $S = 1$ designates the cutoff for variable sources.

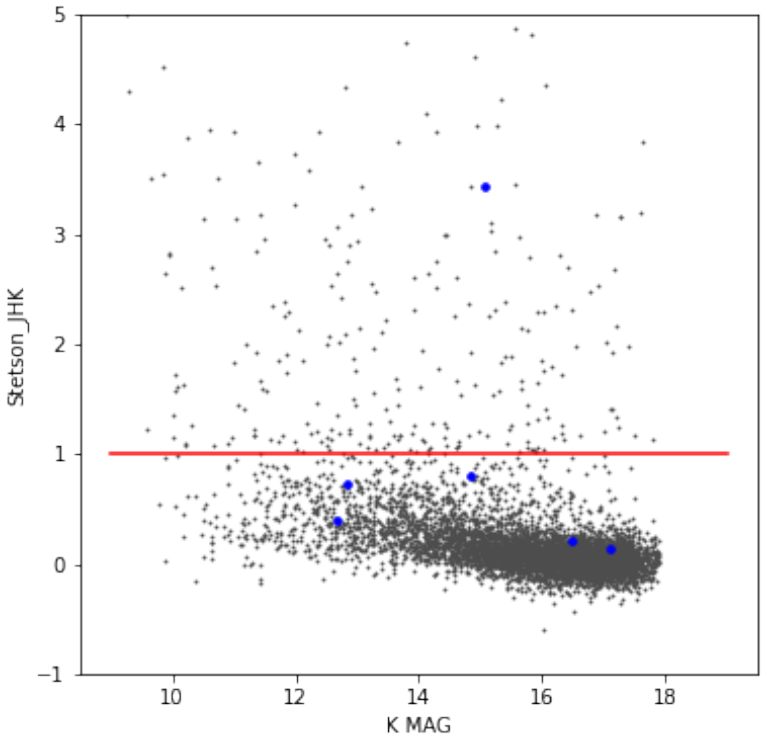

FIGURE 10. Plot of *JHK* Stetson variability index vs *K* magnitude in NGC 1333. All UKIRT sources are shown in gray; all matched sources are shown in blue. A red line at $S = 1$ designates the cutoff for variable sources.

Periodic Variability Analysis

We searched for periodic variability in these sources using the Lomb-Scargle Periodogram [20]. In brief, Lomb-Scargle periodogram analysis searches for sinusoidal signals in an irregularly sampled light curve, displaying a periodogram showing the power of a hypothetical periodic signal at all frequencies of interest. We made use of the periodogram software implementation included within Astropy, see [35].

All 16 sources were searched for periodic signals in each of the three photometric bands. A periodic signal was deemed to be found if a strong peak in all three bands was evident between periods of 1 hour and 100 days, with a false alarm probability (FAP) of 10^{-5} or smaller, which (upon inspection of a light curve folded on the candidate period) passed visual scrutiny. One of the 16 sources (J055 in IC 348, shown in Fig. 3) was identified as periodic in this way. Figure 11 shows the three-band periodogram of this source. Note that the additional, weaker peaks seen to the left and right of the strongest period appear due to the windowing function which arises from the approximately nightly observing cadence of our survey. These spurious peaks are expected in the periodogram of a singly periodic source observed with such a cadence; we refer readers to [34] for further discussion on the interpretation of astronomical periodograms.

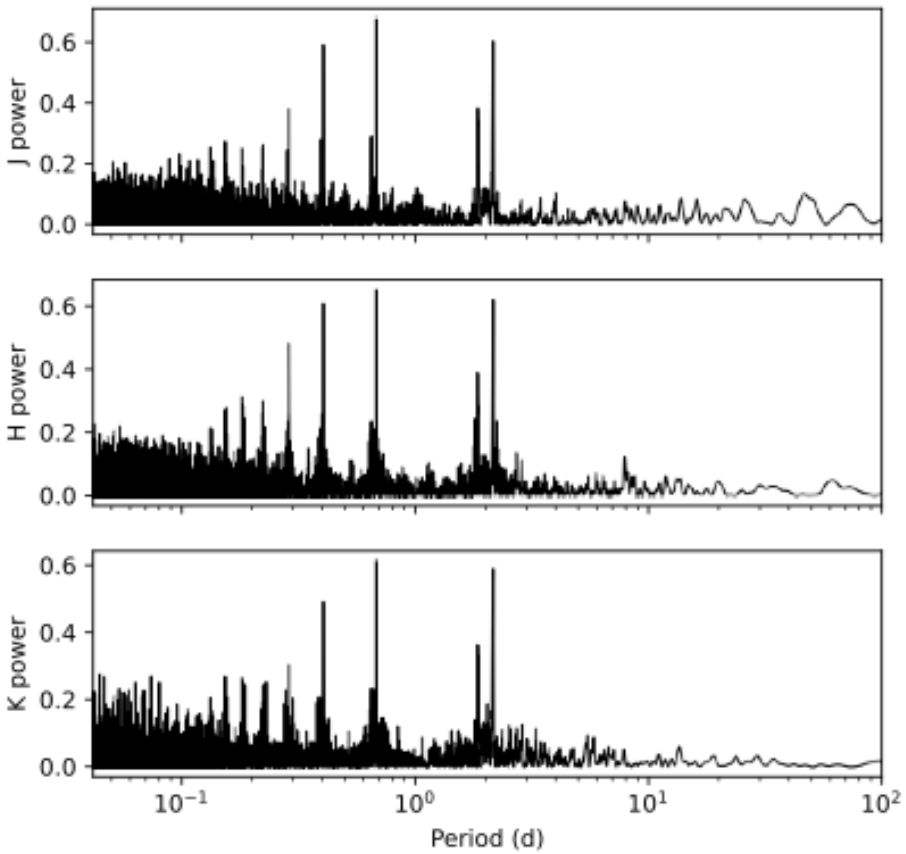

FIGURE 11. Lomb-Scargle periodogram for source J055 in IC 348 (with corresponding light curve shown in Fig. 3). The best-fit period (i.e., with the strongest peak in all three bands) was 0.68171 d. The false-alarm probability associated with this period was 2.15×10^{-9}. The additional, weaker peaks seen in the periodogram are due to the windowing function arising from the approximately nightly observing cadence and are expected.

Variability of Overall Population

TABLE 3. Results of positional matching and variability analysis. The two sources designated as "other" were designated as such because one had magnitudes fainter than the completeness limits and the other was pipeline flagged as having faulty photometry.

	IC 348	NGC 1333
Total Sources Considered	29	12
Positional Matches	10	6
Variables	2 of 10	1 of 6
Periodic Variables	1 of 2	0 of 1
Nonmatches	18	5
Other	1	1

The variability fraction among the matched sample is 3/16 (19%); variability properties of the three discovered variables are given in Table 5. The peak-to-peak (ptp) *K* magnitudes, which are shown in Table 5, are 0.06 for the periodic variable and 0.21 (J056) and 0.26 (J052) for the nonperiodic variables.

Reported variability fractions from similar surveys of low-mass stellar objects and/or BDs range from 11% to ~70% [4, 30, 31, 5, 7]. Our sample population is significantly smaller than the populations assessed in these papers (whose populations are in the 124–3500 range) and therefore has a much larger overall uncertainty. The signal-to-noise ratios calculated here are interrelated with the brightness of each object; this ratio is highly variable across our sample (the error bars vary by as many as 2–3 orders of magnitude). As a consequence of the nonuniform signal-to-noise across our sample, the recorded variability rate of 19% is the lower-limit rate.

TABLE 4. Summary of BD, membership status to regions according to all three catalogs for all 16 positionally matched objects. Some of these sources were previously identified as BDs by [16] and are shown in Tables 1 and 2 of that paper for members of IC 348 and NGC 1333, respectively. Our three variables are shown in bold. Mass estimates in the rightmost two columns make use of the spectral-type-to-temperature conversions given by Luhman et al. in [18] and Herczeg and Hillenbrand in [33], and are denoted L03 and HH14, respectively; all mass estimates use the Baraffe et al. isochrones [17].

Source Name	Source Catalog	Region	SpT	Designated Member by L16?	Est. Mass from L03 (M_{solar})	Est. Mass from HH14 (M_{solar})
UHW J052.43392 +31.32982	**Allers 2020**	**NGC 1333**	**M8**	**Y**	**0.030**	**0.030- 0.025**
UHW J052.40147 +31.29717	Allers 2020	NGC 1333	L0	Y	–	–
UHW J052.35191 +31.47077	Allers 2020	NGC 1333	M6	Y	0.110	0.060
UHW J052.27886 +31.49911	Allers 2020	NGC 1333	M8	Y	0.030	0.025
2MASS J03284022 +3125490	Esplin 2017	NGC 1333	M6	N	0.110	0.060
IRS J03294217 +3117205	Esplin 2017	NGC 1333	M9.5	N	–	–
UHW J056.01221 +31.87436	**Allers 2020**	**IC 348**	**M6**	**Y**	**0.110**	**0.060**
UHW J055.98976 +32.24691	**Allers 2020**	**IC 348**	**M7**	**Y**	**0.060**	**0.035**
UHW J055.76964 +32.16007	Allers 2020	IC 348	M8	N	0.030	0.025
UHW J055.75603 +32.03731	Allers 2020	IC 348	M6	Y	0.110	0.060
UHW J055.73277 +32.07455	Allers 2020	IC 348	M7	N	0.060	0.035
UHW J055.71237 +31.94127	Allers 2020	IC 348	M7	N	0.060	0.035
UHW J056.17321 +32.17758	Allers 2020	IC 348	M6	Y	0.110	0.060
UHW J056.34957 +32.19849	Allers 2020	IC 348	M7	Y	0.060	0.035
IRS J03443516 +3211052	Esplin 2017	IC 348	M9-L3	N	–	–
IRS J03444379 +3213512	Esplin 2017	IC 348	Mid-M?	N	0.170	0.105

TABLE 5. Individual data on each variable. Abbreviations for source names are shown here and used above.

Source Name	Region	Spectral Type	Periodic?	IR Excess?	PtP Amplitude
UHW J052.43392 +31.32982 (J052)	NGC1333	M8	No	Yes	0.26
UHW J056.01221 +31.87436 (J056)	IC 348	M7	No	Yes	0.21
UHW J055.98976 +32.24691 (J055)	IC 348	M6	Yes (P = 0.68 d)	No	0.06